NASA/TM—2012–215996

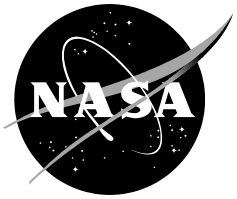

Thermostructural Analysis of the SOFIA Fine Field and Wide Field Imagers Subjected to Convective Thermal Shock

Christopher B. Kostyk

Dryden Flight Research Center, Edwards, California

March 2012

NASA STI Program ... in Profile

Since its founding, NASA has been dedicated to the advancement of aeronautics and space science. The NASA scientific and technical information (STI) program plays a key part in helping NASA maintain this important role.

The NASA STI program operates under the auspices of the Agency Chief Information Officer. It collects, organizes, provides for archiving, and disseminates NASA's STI. The NASA STI program provides access to the NASA Aeronautics and Space Database and its public interface, the NASA Technical Report Server, thus providing one of the largest collections of aeronautical and space science STI in the world. Results are published in both non-NASA channels and by NASA in the NASA STI Report Series, which includes the following report types:

- TECHNICAL PUBLICATION. Reports of completed research or a major significant phase of research that present the results of NASA Programs and include extensive data or theoretical analysis. Includes compilations of significant scientific and technical data and information deemed to be of continuing reference value. NASA counterpart of peer-reviewed formal professional papers but has less stringent limitations on manuscript length and extent of graphic presentations.

- TECHNICAL MEMORANDUM. Scientific and technical findings that are preliminary or of specialized interest, e.g., quick release reports, working papers, and bibliographies that contain minimal annotation. Does not contain extensive analysis.

- CONTRACTOR REPORT. Scientific and technical findings by NASA-sponsored contractors and grantees.

- CONFERENCE PUBLICATION. Collected papers from scientific and technical conferences, symposia, seminars, or other meetings sponsored or co-sponsored by NASA.

- SPECIAL PUBLICATION. Scientific, technical, or historical information from NASA programs, projects, and missions, often concerned with subjects having substantial public interest.

- TECHNICAL TRANSLATION. English-language translations of foreign scientific and technical material pertinent to NASA's mission.

Specialized services also include organizing and publishing research results, distributing specialized research announcements and feeds, providing help desk and personal search support, and enabling data exchange services.

For more information about the NASA STI program, see the following:

- Access the NASA STI program home page at *http://www.sti.nasa.gov*

- E-mail your question via the Internet to help@sti.nasa.gov

- Fax your question to the NASA STI Help Desk at 443-757-5803

- Phone the NASA STI Help Desk at 443-757-5802

- Write to:
  NASA STI Help Desk
  NASA Center for AeroSpace Information
  7115 Standard Drive
  Hanover, MD 21076-1320

NASA/TM—2012–215996

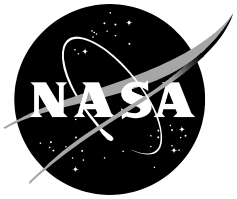

Thermostructural Analysis of the SOFIA Fine Field and Wide Field Imagers Subjected to Convective Thermal Shock

Christopher B. Kostyk

Dryden Flight Research Center, Edwards, California

National Aeronautics and
Space Administration

Dryden Flight Research Center
Edwards, CA 93523-0273

March 2012

Available from:

NASA Center for AeroSpace Information
7115 Standard Drive
Hanover, MD 21076-1320
443-757-5802

Abstract

The Stratospheric Observatory for Infrared Astronomy (SOFIA) is a highly modified Boeing 747-SP (The Boeing Company, Chicago, Illinois) with a 17-ton infrared telescope installed in the aft portion of the aircraft. The SOFIA aircraft can deploy to make observations at any time, anywhere in the world. The originally designed aircraft configuration included a ground pre-cooling system to chill the telescope cavity and optical components, however, that system was not installed. This lack of ground pre-cooling capability was the source of the concern about whether or not the fine field and wide field imagers would be exposed to potentially unsafe thermostructural environments. This concern was in addition to the already-existing concern that the air temperature rate of change during flight (both at a constant altitude as well as in ascent or descent) could cause the imagers to be exposed to unsafe thermostructural environments. Four optical components were identified as the components of concern; two of higher concern (one in each imager), and two of lower concern (one in each imager). The analysis effort began by analyzing one component, after which the analyses for the other components were deemed unnecessary. This report documents the analysis findings and the lessons learned from the effort.

Nomenclature

Al	aluminum
CTE	coefficient of thermal expansion, /K
C_p	specific heat, J/kg-K
DSI	Deutsches SOFIA Institut
E	modulus of elasticity, N/m^2
FEM	finite element method
FFI	fine field imager
G	shear modulus, N/m^2
h	convection coefficient, W/m^2-K
k	thermal conductivity, W/m-K
KT	Kayser-Threde GmbH
LBCs	loads and boundary conditions
M	Mach number
MSC	MacNeil Schwindler Corporation
NASA	National Aeronautics and Space Administration
$q"_{conv}$	convective heat flux, W/m^2
R	recovery factor, 0.9
SOFIA	Stratospheric Observatory for Infrared Astronomy
t	time, s
T	temperature, °C or K
TA	telescope assembly
T_{amb}	ambient temperature at altitude, K
T_f	temperature of the fluid (air at altitude, in this case), °C or K
T_i	initial temperature, K
T_R	recovery temperature, K
T_s	temperature of the structure, K
WFI	wide field imager
α	coefficient of thermal expansion, /K
γ	ratio of specific heats
$\delta_{( )}$	displacement along ( ) coordinate direction

$\Delta( )$ change in ( )
μ coefficient of static friction
ν Poisson's ratio
ρ density, kg/m^3
σ stress, N/m^2

Introduction

The original configuration for the Stratospheric Observatory for Infrared Astronomy (SOFIA) aircraft included a ground pre-cool system, the purpose of which was to chill the telescope cavity and components (fig. 1) on the ground in order to avoid the excessive hold times at altitude that would be necessary to obtain the thermal equilibrium which is a prerequisite for telescope operation. Various factors in the SOFIA project history necessitated the team considering flying open-door flights (flights in which the telescope cavity door is opened at altitude) without having a ground pre-cool system installed in the aircraft.

Of concern was whether or not the absence of ground pre-cooling would present flight conditions under which some of the optical components would be exposed to convective thermal shock conditions, which could generate stresses exceeding safe operating levels. The convective thermal shock scenario is the worst-case scenario, because a shock is the limiting case of increasing cooling rates (that is, a shock is an instantaneous fluid temperature change instead of a finite cooling rate). Furthermore, a cold air "splash" at altitude is potentially more harmful than a descent scenario with the cavity door stuck open because in the descent heating scenario the surface of the optical component is put into compression; additionally, the descent heating rate would be much lower than the cooling rate occurring during the opening of the cavity door at altitude. Secondary to this concern was the concern regarding the telescope cavity air temperature rate of change at altitude during flight (whether or not a pre-cooling system was present) and whether or not that rate of change could cause unsafe stress levels.

Lastly, there was a minor concern regarding the steady-state condition with the coefficient of thermal expansion (CTE) mismatch between the glass components and their metal mounting structures. This concern was found not to be a problem because the imagers had been thermally ground tested using a very slow cooling rate of 0.2 °C per minute to a steady-state temperature (-70 °C), which is colder than what would be seen in flight.

Four different optical components were identified as being of concern. Two were identified as much more critical: the Schmidt Plate in the fine field imager (FFI); and the Achromat 1 in the wide field imager (WFI).Two were identified as less critical: (the Achromat in the FFI, and the Achromat 2 in the WFI). The Schmidt Plate was the first and only component analyzed. This approach was taken because the Schmidt Plate, being held in place by a strong clamping mechanism not present in the other three optical components,[1] was very clearly the most heavily loaded of the four. Additionally, only the two components identified as being of higher concern were exposed to the cold blowing air at altitude; the other two components were located inside the imagers and were therefore subjected to a much more benign thermal environment. After the Schmidt Plate analysis it was clear that an analysis effort for the other three components would not be necessary.

[1] The other three components are secured in fixtures by hand-tightening a ring on top of the optic, and then hand-tightening a fixing ring behind that ring to hold the optic in place.

This report summarizes the conservative examination of the stress levels generated in the FFI Schmidt Plate, and the resulting implications for the stress states in the other three identified components. This report documents these findings and the lessons learned from the effort.

Description of the Problem

A critical step in the modeling process is the careful consideration of all significant physics that must be included in the model. In the case of the Schmidt Plate in the FFI, any effect that contributed to either the thermal or structural response needed to be modeled. Figures 1-3 give a sense of how the Schmidt Plate is installed in the aircraft.

The forward portion of the aircraft is to the left in figure 1. The air flows over the forward portion of the cavity opening and into the cavity, passing over the imagers. The baffles[2] for the FFI and WFI can be clearly seen in figure 1; figure 2 shows that the baffles are mounted to the headring, with the imagers installed behind the headring. Figure 3 shows a cutaway view of the FFI without the baffle. The 120-deg sector of the front portion of the FFI that was modeled is shown in figure 4(a).

The potential thermal and structural loads experienced by the Schmidt Plate and their initial consideration are summarized in table 1. In addition to the table, a few words of explanation will help in understanding the loads listed. Load numbers 1 and 2 are very clearly negligible because the Schmidt Plate has a mass of approximately 1.14 kg (2.5 lb). Load number 3 is clearly negligible because the entire telescope assembly (TA) is vibration isolation mounted. Load number 4 is clearly negligible because the pressure oscillation in the TA cavity due to acoustic waves at the worst resonance condition would only be 413 Pa (0.06 psi). Load number 5 is thermal stress that is caused by the transient cooling condition in which the surface of the glass is convectively cooled, and due to its low thermal conductivity the internal temperature of the glass has a thermal response that significantly lags behind that of the surface (that is, it remains warm). In this scenario a surface tension results, which is a concern because glass is very strong in compression, but not very strong in tension.[3] This is especially true for the more severe convection on the outer face of the Schmidt Plate, as opposed to the free / low-speed convection on the internal surface of the Schmidt Plate. Load number 6 in the table is referring to the circumferential (hoop) clamping due to the contraction of the metal mount around the Schmidt Plate (which has a lower CTE). Load number 7 is the stress caused by the clamp that holds the Schmidt Plate in the FFI, and any resulting increase or decrease in the clamping force due to CTE mismatch.

[2] The purpose of the baffles is purely to block out stray light from the imagers.

[3] Per conversation with a Schott employee. Furthermore, the tensile strength of glass is almost entirely dependent on its surface finish, and almost independent of composition. Fortunately, in this case, the glass under consideration has an optical surface finish (it is very highly polished, indicating higher strength). This finish is not everywhere on the glass (that is, not on the edges or circumferential surfaces); however, the portions of glass exposed to cooling are the optically-finished surfaces.

Table 1. Preliminary assessment of the potential loads to be modeled.

Load	Significance
1. 1g	Negligible
2. 4g (or other) maximum flight load	Negligible
3. Vibratory stress	Negligible
4. Acoustic pressure	Negligible
5. Thermal stress (cooling-induced gradient)	Uncertain, potentially significant
6. Circumferential clamping (CTE mismatch)	Uncertain, potentially significant
7. Clamp pre-load +/- CTE mismatch	Uncertain, potentially significant

After discussing the necessary physics to include in the model, the next topics of consideration are what results would be of interest and what stress levels would be acceptable. As mentioned in the description of Load number 5, the surface tension was the obvious failure mode with which to be concerned; the decision was made to consider the maximum principal stress the quantity of interest. A technical report on the Web site of the glass manufacturer stated that for a comparable glass an allowable tensile stress of 10 MPa (1.45 ksi) would be sufficiently low that *regardless of composition or surface finish* (emphasis added) (as long as there was no major damage to a surface or edge) a component would not fail either instantly or over time from fatigue (ref. 1). Furthermore, the technical report shows data for the characteristic strength values of many different types of glass, and the corresponding fracture probability. These data comparatively show just how conservative is the 10-MPa allowable stress value.[4] Additionally, reference 1 also states that applications requiring higher stress levels should apply the statistical method described in the document to determine allowable stress levels. The data provided showed that zero failure probability stress levels (regardless of surface finish) did not reach 20 MPa for any of the sample glass types, therefore a 20-MPa allowable stress was also considered conservative. The 20-MPa stress limit was therefore seen as a benchmark value and not an absolute limit. Clearly, if the analyses returned stress levels below or near the reported allowable stress value, the concern about thermal-shock-induced stress would be relieved. Furthermore, because the FFI had already been successfully tested in a laboratory setup utilizing extremely slow cooling rates, the chief result coming out of the analyses was a comparison of the magnitudes of maximum principal stresses generated by the clamping mechanism and by the thermal effects. This comparison would have numerous implications, not only for the Schmidt Plate but also for the other three components of concern.

Finally, as is hinted at in table 1, there are multiple sources of uncertainty in this problem. Therefore, it was understood that in order for this analysis effort to be complete, the analysis needed to be a series of parameter sensitivity studies, which would have two benefits. First, confidence would be established in the understanding of the bounds on what stress levels could be induced given exposure to the most extreme operating conditions. Second, a tool would be produced for the project team's use. The team's tool could be used to quantify the effects of different amounts of conservativism and what proportionality there was to each parameter in the results. The tool could also be used during the life of the project to estimate what stress levels might be imparted given whatever combination of parameters are present in a given flight.

[4] In some cases there is a factor of four between the zero fracture probability strength and the 10-MPa value; in other cases this factor is even higher.

Determination of the Governing Parameters

This was not a quickly solved problem, because there were many questions that needed to be answered prior to creating a computer model. Clearly, engineering discernment was necessary to determine what portion of the platform needed to be modeled, with the desire being to limit computational expense by limiting the components involved while still capturing the necessary physics. The implication has already been made that the material properties and strength values could not be so simply obtained as by looking them up in a textbook. Additionally, the standard effort to determine structural and thermal loads and boundary conditions required engineering judgment and calculation.

Geometry

Before gathering the material properties and calculating the loads, the relevant control volume must be discerned. For this problem, based on the structure and location in the aircraft of the FFI (figs. 1-3), the control volume was considered to include most of the FFI front group, which provides the loading and boundary conditions for the Schmidt Plate. Figure 4(a) shows the parts included in the final axisymmetric 120-deg sector model. The engineering drawings were consulted for the dimensions for the mount, pressure ring, clamp, Schmidt Plate alignment ring, and bolt. No drawings were consulted for the Schmidt Plate, as it is an off-the-shelf item. Dimensions were obtained from Kayser-Threde GmbH (KT) (Munich, Germany), the designer and manufacturer of the imagers.

Material Properties

Once the relevant geometry was determined, the engineering drawings for the parts were consulted for material identification, excepting, as indicated, the Schmidt Plate. Testing the glass resulted in a list of possible glass types, all of which had similar properties. The Deutsches SOFIA Institut (DSI) (Stuttgart, Germany), KT, and the National Aeronautics and Space Administration (NASA) agreed that the NBK-7 properties would be the conservative values that would be used (Technical Interchange Meeting Summary Notes, Munich, May 4-6, 2009). The aluminum (Al) and stainless steel (SS) material properties for AL 5005 (the mount), Al 6061 (the clamp), Al 7075 (the pressure ring and the Schmidt Plate alignment ring), and SS 301 (the bolt) were all found using an online database located at www.matweb.com. The intent was to refine these properties should the analyses return values with sufficiently small (or negative) margin to necessitate increasing the fidelity of the calculations. The values used are shown in tables 2 and 3.

Table 2. The mechanical properties used in the analyses.

Material	E (N/m^2)	G (N/m^2)	ν
Al 5005A	6.89E+10	2.59E+10	0.33
Al 6061	6.89E+10	2.59E+10	0.33
Al 7075	7.17E+10	2.69E+10	0.33
SS 301	2.1E+11	8.08E+10	0.3
NBK-7	8.2E+10	3.4E+10	0.206

Table 3. The thermal properties used in the analyses.

Material	ρ (kg/m^3)	α (1/K)	k (W/m-K)	C_p (J/kg-K)
Al 5005A	2700	2.38E-5	200	900
Al 6061	2700	2.36E-5	170	896
Al 7075	2810	2.36E-5	155	960
SS 301	8000	1.6E-5	16.2	500
NBK-7	2510	7.1E-6	1.114	858

Structural Loading

The structural loading consists of the bolt pre-load on the clamp; see figure 4(b). The bolt pre-load is transmitted to the Schmidt Plate through the clamp, which then transmits load to the Schmidt Plate as it is held between the pressure ring and the Schmidt Plate alignment ring (which rests on a ledge on the mount). The range of pre-load values to be used in the analysis was agreed to be 2,000 to 3,000 N (personal correspondence with Karl-Heinz Zuknik of KT, August 10, 2009). It is the opinion of the analyst that the lower bounding value for the pre-load range is closer to the real value than is the upper bounding value, which is seen as a conservative value.

Thermal Loading

The conservative approach to the thermal loading can be described simply as convective thermal shock. With constant temperature (conductive) boundary conditions the maximum gradient, and therefore thermal stress, occurs at the onset (t = 0); however, with convection boundary conditions at t = 0, the structure is still at T_i. The maximum thermal gradient in the structure occurs at some finite time t > 0. A transient analysis is therefore required. Two parameters control the thermal shock severity: the shock strength (T_s - T_f), and the convection coefficient. The necessary parameters to define, therefore, are the initial temperature, fluid temperature, and convection coefficients.

Initial Temperature

Although this aircraft is planned for deployment around the world as a mobile observatory (thus being exposed to many different ground thermal environments), the expectation of using the environmental control systems already onboard the aircraft in a mode to get the telescope cavity down to an initial structural temperature of, at most, 20 °C is very reasonable and realistically conservative. Obviously, the colder the initial structural temperature, the lower the thermal shock (and, therefore, stress).

Fluid Temperature

The temperature of the TA cavity air will not be the ambient temperature at altitude once the cavity door opens, but, rather, will be the recovery temperature. The recovery temperature was calculated according to equation (1), (internal memo from Horn and Meyer, University of California at Los Angeles, 2000):

$$T_R = \left[1 + R\frac{\gamma - 1}{2}(M - 0.1)^2\right] T_{amb} \quad (1)$$

where T_R is the recovery temperature; R is the recovery factor; γ is the ratio of specific heats; M is the Mach number; and T_{amb} is the ambient temperature at altitude.

The $(M - 0.1)^2$ quantity is used in place of the traditional M^2 because the air around the imagers will not have slowed to zero velocity[5] (a very conservative value from those presented in an internal memo from Sven Schmid, DSI, July 14, 2008). In order to obtain a conservative value for T_R the conservative combination of independent variables was selected. The aircraft is planned to fly up to approximately 40,000 ft (12,200 m). Most tables list the temperature at this altitude to be -57 °C. Using the above equation with M = 0.76 yields a conservative value of T_R = -40 °C.[6] As such, the nominal worst possible temperature difference ($T_s - T_f$, where $T_f = T_R$) for the convective thermal shock is approximately 60 °C, if no significant cooling occurs during the ascent and the cavity door is opened at altitude.

It should also be noted that the fluid temperature was assumed to instantaneously change to the recovery temperature once the cavity door opens. Although there is a large fluid volume in the TA cavity, both imagers are located on the TA headring and are close to the opening. Making the assumption that the fluid temperature instantaneously changes to T_R is seen as not only a conservative approach, but is in fact the limiting scenario: there can be no worse condition, only less severe, given any finite rate of change.

Convection Coefficients

To accurately calculate a convection coefficient requires accurate knowledge of the geometry and the flowfield on and around the object being analyzed; see figure 4(c). In this case, both the geometry and the flowfield are complex.

The flow over the imagers can be described by two components. The first component is the flow that occurs inside the baffle, over the front surface of the imager. The second component is the low-speed flow that occurs around the body of the imager, which is protected behind the headring. It is unknown how the flow will enter the TA cavity over the forward edge of the opening; it is further unknown what flow this will cause inside the baffle of the imager. Although this flow may be difficult to visualize for the reader not intimately acquainted with the TA geometry, the description that follows of the conservative flow approach will be simple to visualize.

It was deemed prudent to use a number of different convection coefficient correlations (subsonic stagnation point, laminar and turbulent flat plate, laminar and turbulent low-speed flat plate, and two different methods for free convection) and choose the most extreme value (refs. 2 and 3). As would be expected, the subsonic stagnation point correlation returned the highest convection coefficient value. Additionally, as the correlations require altitude conditions to perform the calculations, the two altitude extremes set by the project office (15,000 ft or 4,600 m, and 40,000 ft or 12,200 m) were used for each correlation. Again, as would be expected, the convection coefficients calculated at the 15,000-ft altitude were higher. The highest convection coefficient calculated (the subsonic stagnation point at 15,000 ft) was found to be 59.5 W/m^2-K.

Apart from the flow in the baffle impinging on the Schmidt Plate, there is free convection inside the imager, as well as low-speed flow around the housing. After calculating the low-speed and free

[5] The value of 0.1 used for a residual Mach number is very conservative from both a computational fluid dynamics (CFD) perspective and a flight data perspective. The flight data indicate that a value between 0.015 and 0.03 would be much closer to the real residual flow velocity. In the interest of conservativism the largest nearby value from Sven Schmid's CFD results was used; his memo presented values that were much closer to the flight data.

[6] The slower the vehicle travels, the less energy will be put into the flow, which means that the coldest recovery temperature would occur at the stall speed. At 40,000 ft the stall speed recovery temperature value is approximately -56 °C. The vehicle will not be travelling near the stall speed, so this value was seen as overly conservative. The thermal shock strength this could generate, however, is covered inside the bounds of the parameter sensitivity study that was performed.

convection correlations, the value of 5 W/m^2-K was chosen for the internal surfaces of the Schmidt Plate as well as for the portions of the housing that see flow.

It should be noted that using the highest convection coefficient found (subsonic stagnation point at 15,000 ft) (4,600 m) with the lowest T_R possible (at 40,000 ft) (12,200 m) is an unrealistically harsh calculation (is physically impossible) and is therefore conservative in the extreme. For comparison, at 15,000 ft (4,600 m) $T_{amb} \approx -15$ °C (according to most standard atmosphere tables), leading to a $T_R = 5$ °C and therefore a ΔT value of 15 °C; whereas at 40,000 ft (12,200 m) $h_{subsonic}$ stagnation ≈ 30. It can be seen that if altitude-appropriate paired values of ΔT and h were used the higher ΔT would be paired with an h value that is half of the value at the lower altitude, while the higher h value would be paired with a ΔT value that is a quarter of the value from the higher altitude. This method was seen as an important element of conservativism in performing the analyses. Making the analyses extremely conservative was seen as important because this effort is seeking to show margin above the realistically worst possible scenarios, and thus provide risk reduction.

Finite Element Method Modeling

The first analyses performed were hand calculations, which provided the bounding values to help in developing the finite element method (FEM) models. Assuming that an infinitely thin surface layer becomes a new temperature instantaneously and is directly above another infinitely thin layer that remains at the initial temperature, the thermal stress generated is $\sigma = E \alpha \Delta T$. Performing this calculation for the Schmidt Plate with $\Delta T = 60$ °C yields a thermal stress of 34.9 MPa.

The first FEM models made were two-dimensional (2-D) and three-dimensional (3-D) transient thermal models using MSC.PatranThermal (MSC Software, Santa Ana, California) as the solver. There were several benefits to performing these simpler models first. One benefit was to gain an understanding of the heat flow through the components. A second benefit was to observe the point at which the thermal gradient was at its maximum. If this analysis were only concerned with the worst gradient, this knowledge would provide for greatly reduced run times. It was uncertain, however, whether or not the CTE mismatch between the glass and the housing would be a dominant component of the overall stress state. Therefore, this benefit did not translate into reduced run times, because the model needed to be run to its steady-state solution (or at least reasonably close to it) in order to determine when the overall stress state was at a maximum (at a transient peak, or at the steady-state solution). The analysis did translate into a better understanding of a critical behavior of the model. A third benefit was that this method allowed simple, fast models for testing different boundary conditions and their relative effects.

During the early 2-D and 3-D transient thermal analyses it was realized that the structural models needed to be 3-D due to the need to model the pre-loaded clamp mechanism. Also during these early analyses, it was realized that degrees of freedom needed to be allowed at the interface of the components in the structural models due to their CTE mismatch and attachment method (that is, the components were clamped, not bolted or bonded). If the mesh were to be continuous across the components there would be a false shear imparted at the interface of the metal and the glass that is not present in reality. This realization led to the pursuit of contact modeling. Contact modeling involves the definition of contact bodies, with the nodes of one body interacting with the elements of another body using appropriately defined contact parameters (that is, friction coefficients, thermal resistance, contact tolerance, et cetera). An image of the model with the contact bodies color-coded is provided in figure 4(a). As well, during the early 2-D and 3-D transient thermal models there were some nodal temperature distributions taken over to structural meshes for early thermal stress estimates. It was obvious that if a coupled thermal and structural analysis could be performed, significant time could be saved, especially given the requirement to perform

a parameter sensitivity study. The desire for a 3-D coupled thermal-structural transient FEM model that included thermal and structural contact led to the selection of MSC.Marc, (MSC Software, Santa Ana, California) as the solver, with MSC.Patran as the pre- and post-processor.

The final FEM model incorporated all of the input parameters defined above, as well as structural constraints. Two structural constraints constrained the model in all three axes. The first constraint prescribed zero displacement in the θ direction for the two side faces of the 120-deg sector (using a cylindrical coordinate system defined at the center of the axisymmetric assembly) effectively constraining the rigid body motions in the Y and Z global coordinate axes. The second constraint prescribed zero displacement in the axial direction (the Z axis in the cylindrical coordinate system, the X axis in the global coordinate system) in the global Cartesian coordinate system (applied at the bottom surface of the mount, away from the region of interest), fully constraining the model.

As in most model development efforts, once this perceived final model was envisioned there were numerous iterations before the model was run successfully. There were several distractions from the main problem, but the primary lesson learned was more the result of an oversight. The mesh in the contact regions of the clamp, pressure ring, Schmidt Plate, and Schmidt Plate alignment ring needed to be dense enough so that there were enough nodes in contact at any time to keep the load transfer uniform. For example, if the pressure ring were only one element deep (in the radial direction) and the inner nodes were to go out of contact, then all of the load would be transmitted only through the outer nodes, and the resulting false stress concentration would raise the stresses to an artificially high level.

After the model was running successfully, to get the contact body portion of the model to run correctly required what amounted to a mesh refinement study. While the model *was* working, the mesh refinement was performed to get that portion of the model working, *not* demonstrating convergence toward the real solution. Thus, there had been a false sense of sufficiency in the model development process. After this realization another mesh refinement was performed in the contact region (the region of higher gradients, which is the region of interest) to determine solution convergence. Element volume was reduced 80 percent and then another 15 percent. The first element reduction led to a reduction in static loading maximum principal stress of 3.8 percent (from 10.6 MPa to 10.2 MPa). The second element reduction produced a less than 1 percent change in static loading maximum principal stress. The change was not, however, monotonic, as the static loading maximum principal stress was 10.3 MPa. This condition was not perceived to be a problem because the element size was quite small at this point due to the diminutive dimensions of the pressure ring and Schmidt Plate alignment ring, seen in figure 4(a), and numerics likely played a role in the small change. The final mesh refinement therefore demonstrated that the original model produced results within 5 percent of the much more refined models, and would produce results of sufficient accuracy.

The working model, containing approximately 16,000 hex elements with approximately 21,800 nodes, was used to iterate on several different parameters. Table 4 details the different parameter variations performed. Where table 4 lists the convection coefficient and how it was varied, this is only referring to the convection coefficient for the top surfaces of the Schmidt Plate, clamp, bolt, pressure ring, and mount. The low-speed / free convection coefficient used for the internal surfaces was not varied, because the effect is understood to be negligible.[7] For the thermal shock strength variation (table 5), those fluid temperature changes were applicable to all convecting surfaces (whether high or low convection).

[7] Typical h values for forced convection (gas) are 25 to 250 W/m^2-K whereas free convection values are 2 to 25 W/m^2-K – an order of magnitude difference between the two (ref. 3). Whether free or low-speed convection, the difference in the convection coefficients between the front and side surfaces of the imager is close to an order of magnitude.

Table 4. Summary of the parameter variations used for the parameter sensitivity study.

Load case ID	h	ΔT	Pre-load, kN	$\mu_{Al\text{-}Al}$	$\mu_{Al\text{-}steel}$	$\mu_{glass\text{-}metal}$
00	59.5	60	3	0.5	0.6	0.7
01	59.5	60	2	0.5	0.6	0.7
02	59.5	60	3	1.0	0.6	0.7
03	59.5	60	3	0.2	0.2	0.1
04	59.5	90	2	0.5	0.6	0.7
05	59.5	30	2	0.5	0.6	0.7
06	80	90	2	0.5	0.6	0.7
07	40	90	2	0.5	0.6	0.7

Table 5. Summary of the key results of the parameter sensitivity study.

Load case ID	Pre-load induced stress, MPa	Maximum principal stress, MPa	Time of maximum principal, s
00	15.8	16.8	19.5
01	10.6	11.6	18
02	15.8	n/a	n/a
03	15.8	16.8	19.5
04	10.6	12.14	24
05	10.6	11.14	25.5
06	10.6	12.5	22.5
07	10.6	11.77	22.5

Each model was constructed to run in the same manner. The first load step was a non-linear static analysis that calculated the stress resulting from the specified bolt pre-load. The resulting stress state of this load step was then used as the initial state for the second load step. The second load step was a transient analysis which kept the LBCs from the first load step and added the thermal boundary conditions. This load step performed weakly coupled[8] transient thermal and structural calculations. This process allowed simple separation of the pre-load induced stress from the thermal effects.

Results

The results of the analyses are summarized in table 5 and figures 5-13. The analyses can be broken into four sets; each set illustrates the maximum principal stress sensitivity to variation in pre-load, friction coefficients, Schmidt Plate top surface convection coefficient, and thermal shock strength. The curve fit equations in figures 6, 9, and 11 provide a simple tool to allow calculation of the variation in maximum principal stress at any time, given variations in the independent parameters.

[8] "Strongly coupled" refers to thermal and structural equations being solved simultaneously; "weakly coupled" refers to thermal and structural equations being solved sequentially over several steps; and "uncoupled" refers to the calculations being run independently (that is, a thermal run produces a nodal temperature distribution which is then mapped onto a structural mesh so that a structural run may be performed).

Variation in Pre-Load

Figure 5 shows the maximum principal stress evolution and its sensitivity to pre-load. As seen in table 4, the only parameter that was varied from load case 00 to load case 01 was the pre-load being decreased from the upper bounding value of 3 kN down to the lower bounding value of 2 kN. Table 5 shows that the values of 15.8 MPa and 10.6 MPa, respectively, are not far off from the 10-MPa infinite-fatigue-life stress listed by Schott. Thus, the decrease in maximum principal stress induced in the Schmidt Plate was shown to be quite proportional to the decrease in pre-load (fig. 6).

Several observations can be made from this first parameter variation. First, the *very* conservative nominal scenario of a thermal shock of 60 K with 59.5 W/m^2-K as the top surface convection coefficient produced only a small increase in the maximum principal stress at any time in the Schmidt Plate (1 MPa for both the 00 and 01 load cases) over the pre-load induced level. Second, the maximum value occurred approximately 20 s after the onset of thermal shock. A third observation is that the steady-state stress state is slightly below the initial pre-load stress state due to CTE mismatch. Based on this first comparison it can be seen that the majority (greater than 90 percent) of the maximum principal stress at any time in the Schmidt Plate is caused by the clamping mechanism. The thermal environment contributes only a minor amount of the stress state even with these extremely conservative convective thermal shock parameters. Positive margin results for the range considered.

Variation in Friction Coefficients

As the friction coefficients were inputs to the contact analysis there was a desire to see how they affected the stress state. Load cases 00, 02, and 03 had all inputs in common (3 kN pre-load, 60 K thermal shock strength, 59.5 W/m^2-K top convection coefficient) except the coefficients of friction. Changing the friction coefficients between the parts did not affect the stress state in the Schmidt Plate as one would expect (fig. 7).[9] Positive margin results for the range considered.

Variation in Convection Coefficient

Figure 8 shows the evolution of the maximum principal stress at any time in the Schmidt Plate as it varies with the convection coefficient. As can be seen in table 4, load cases 04, 06, and 07 had all inputs in common (2 kN pre-load, 90 K thermal shock strength, and friction coefficients) except the top surface convection coefficient, which was increased to 80 W/m^2-K in load case 06 and decreased to 40 W/m^2-K in load case 07. The flow configuration is low-speed, thin air at altitude and not steady stagnation flow (as was assumed for the convection coefficient calculation to obtain the most conservative value). Covering this range of values in the sensitivity study should be seen as very conservative. The thermal shock strength was kept at 90 K to dramatically show how insensitive the stress state is to the variation in the convection coefficient. Figure 9 shows the maximum principal stress at any time with the variation in convection coefficient, and table 5 shows the maximum value occurring at close to the same time (just after 20 s). The relationship is shown to be highly linear, with the difference between the pre-load induced maximum principle stress and the trendline solution for h = 0 being only 4 percent off from the pre-load

[9] The observant reader will notice that load case 02 is not plotted in figure 7. Load cases 00 and 03 were allowed to run the full transient analysis for a first comparison. The comparison between load cases 00 and 03 showed that the friction coefficients did not affect the behavior of the model, so the decision was made to not run load case 02 for a transient solution because that run would have tied up the computer for more than a day of unnecessary calculations.

(alone) value.[10] The correlation coefficient clearly shows the linear nature of the relationship. More significantly, the trendline shows that the variation of h from 0 to 80 W/m^2-K produces a change in maximum principal stress at any time in the Schmidt Plate of only 1.5 MPa – and that with an overly-conservative 90-K thermal shock strength. The variation would be less with a smaller, more realistic thermal shock, such as the conservative value of 60 °C that was chosen as nominal in these analyses. Ample positive margin results throughout the range considered.

Variation in Thermal Shock Strength

Figure 10 shows the time history of the stress evolution with variation in thermal shock strength. Table 4 shows that the input parameters to load cases 01, 04, and 05 were all the same (2 kN pre-load, 59.5 W/m^2-K top surface convection coefficient, and friction coefficients), except for the thermal shock strength, which was increased to 90 K in load case 04 and decreased to 30 K in load case 05. The maximum principal stresses all occurred close to 20 s (table 5). In figure 11 the correlation coefficient of the trendline shows the highly linear relationship between the maximum principal stress at any time and the variation in thermal shock strength.[11] As with the variation in the convection coefficient, the span of thermal shocks (from 0 to 90 K) produced a variation in maximum principal stress at any time of only 1.5 MPa. It should also be noted that this is given the use of the extremely conservative subsonic stagnation point convection coefficient. With a lower, more realistic convection coefficient this variation would be less.

Figures 12 and 13 clarify why figures 8 and 10 do not look the same. Although from a thermal perspective the convective heat flux equation $q"_{conv} = h (T_s - T_f)$ shows proportionality to both h and ΔT, the variation in the two quantities are two fundamentally different thermostructural problems. This can be seen by examining the surface temperature time histories. Figure 12 shows that as the structure cools from its initial temperature down to the fluid temperature (in this case $0.7T_i$ for all three load cases) the response is faster with the higher convection coefficient. All of the curves, however, are bound for the same steady-state solution: the same final thermostructural state which has no thermal gradient-induced stress but has the same maximum CTE mismatch effect. Figure 13 shows that not only does the stronger thermal shock cause a more rapid cool-down of the surface (and thus higher stress), but it also leads to a different final thermostructural state ($0.8T_i$, $0.7T_i$, and $0.9T_i$) for each load case. Accordingly, figure 10 shows that the relief due to CTE mismatch (however slight) is greater for the stronger thermal shock, with the corresponding trend following for the other two thermal shocks. Ample positive margin results throughout the range considered.

Conclusions

The parameter sensitivity study provided numerous observations; among them are two key results. The first key result is the understanding of the relative magnitudes of the contribution to the maximum principal stress by the clamping mechanism (greater than 90 percent) as compared to the contribution from very conservative thermal effects (a “small bump”).

[10] In theory h = 0 is not real. As the convection coefficient is decreased, the temperature difference $(T_s - T_f)$ does not disappear; forced convection simply becomes free convection ($h \neq 0$) as flow decreases toward zero velocity. The pre-load (alone) value was calculated as a part of each analysis, since the first load step was always the pre-loaded clamp, and the second load step was the addition of the thermal effects. As such, there is no separate load case associated with these results in table 5.

[11] As with the convection coefficient variation data, the data point for a thermal shock $(T_s - T_f) = 0$ is the stress state with the pre-loaded clamp and no thermal effects.

The second key result is the understanding of the small, linear variation in the already-small thermal contribution to the maximum principal stress state given large perturbations in the two thermal parameters: convection coefficient, and thermal shock strength. As well, any step away from the conservative assumptions (and closer to reality) would be driving the “small bump” to be even smaller. Perhaps the most important outcome was the confidence in the results given that each parameter variation led to positive margin (with respect to the 20-MPa allowable stress benchmark value) throughout the range considered.

Based on these two key results it is obvious that, given the range of foreseeable physically possible thermal environments, even without a ground pre-cooling system installed in the aircraft the Schmidt Plate will never be subjected to a convective thermal shock scenario that could generate a stress state that would either damage it or consume significant fatigue life.

Furthermore, as stated in the “Introduction” section above, none of the other components of concern (in the wide field imager or in the fine field imager) are clamped in place in the same manner as is the Schmidt Plate. The range of possible stress states in the other components, therefore, is well below levels of concern for either damage or fatigue life considerations.

It is therefore concluded that, for any flight, the absence of a ground pre-cooling system (while perhaps posing other programmatic difficulties) does not pose a risk to the optical components in either of the imagers.

The last conclusion concerns model development. On several occasions, consultants from other organizations instructed the author that the element size did not need to be as fine as that which was used. These assertions were based on experience from structural modeling and thermal modeling. Each time, these assertions proved incorrect, as the multi-disciplinary model incorporating contact required a finer mesh. The related conclusion is twofold: it is important to keep careful track of progress made toward a proven, converged solution; and, a sense of mesh density sufficiency for a given type of modeling may no longer apply when increasing the complexity of what is modeled. It is always incumbent upon the analyst to ensure the solution is converged and of sufficient accuracy.

Acknowledgments

The author thanks the personnel at Kayser-Threde GmbH (particularly Markus Erhard and Karl-Heinz Zuknik) for their assistance in providing the information necessary for the analyses, and for their positive attitude throughout the effort. The author also acknowledges the assistance of Pedro Chou of the MacNeil Schwindler Corporation for his assistance during the course of this analysis.

Figures

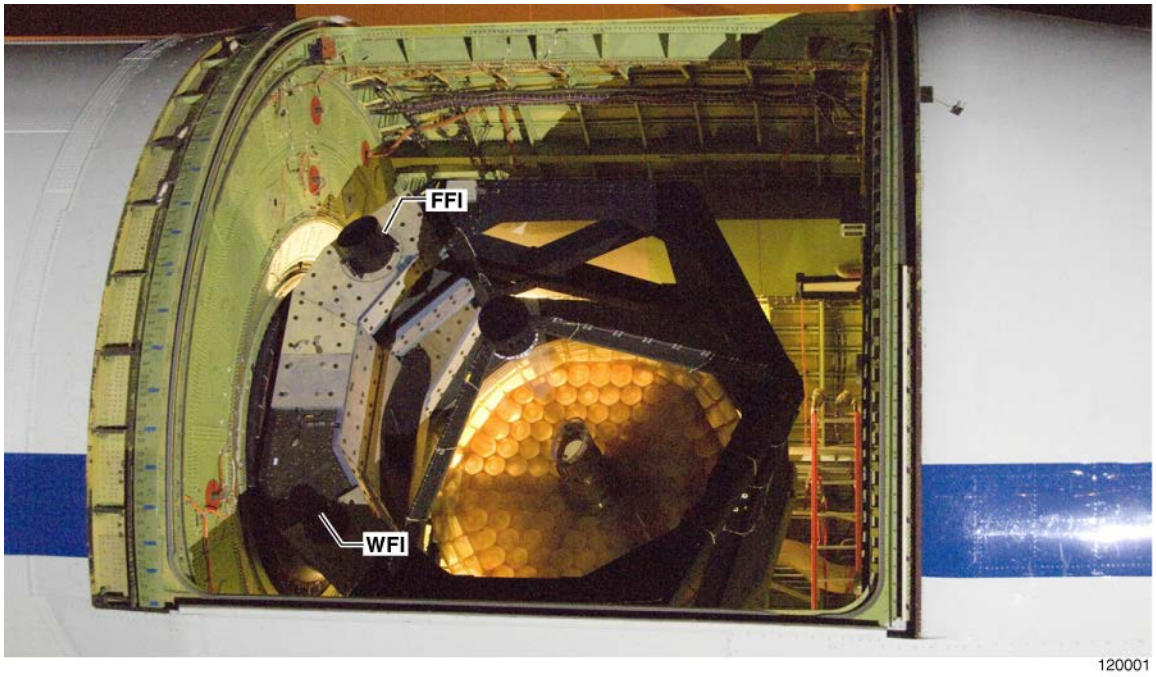

Figure 1. The telescope cavity and telescope assembly (with imagers labeled) installed in the Stratospheric Observatory for Infrared Astronomy.

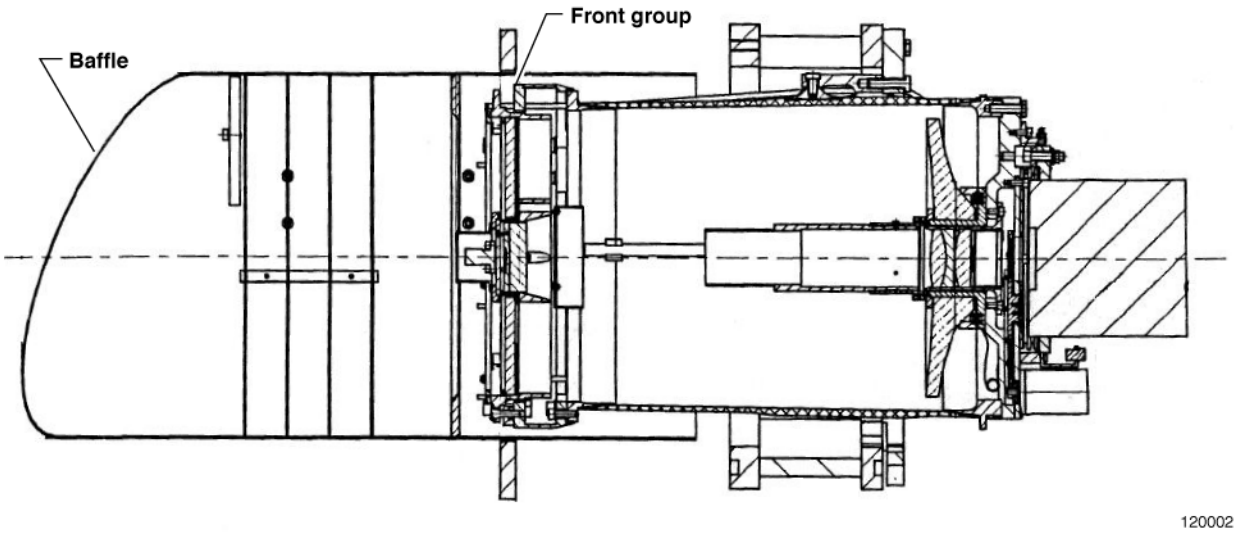

Figure 2. Side view of the fine field imager with the baffle and without the headring structure.

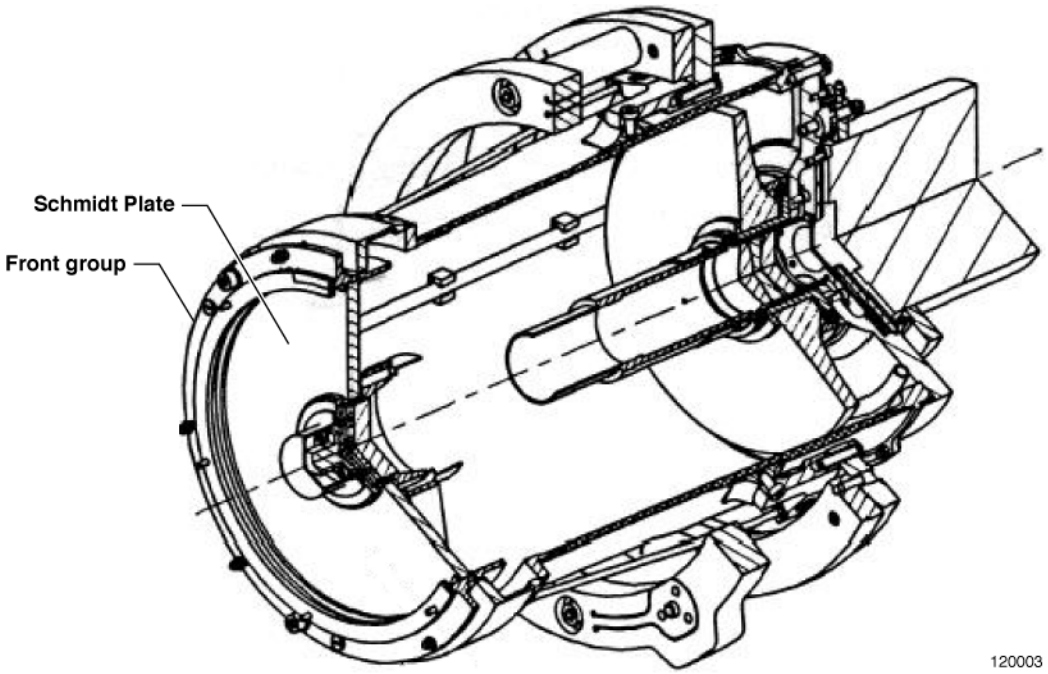

Figure 3. Cutaway view of the fine field imager without the baffle, showing the Schmidt Plate installation.

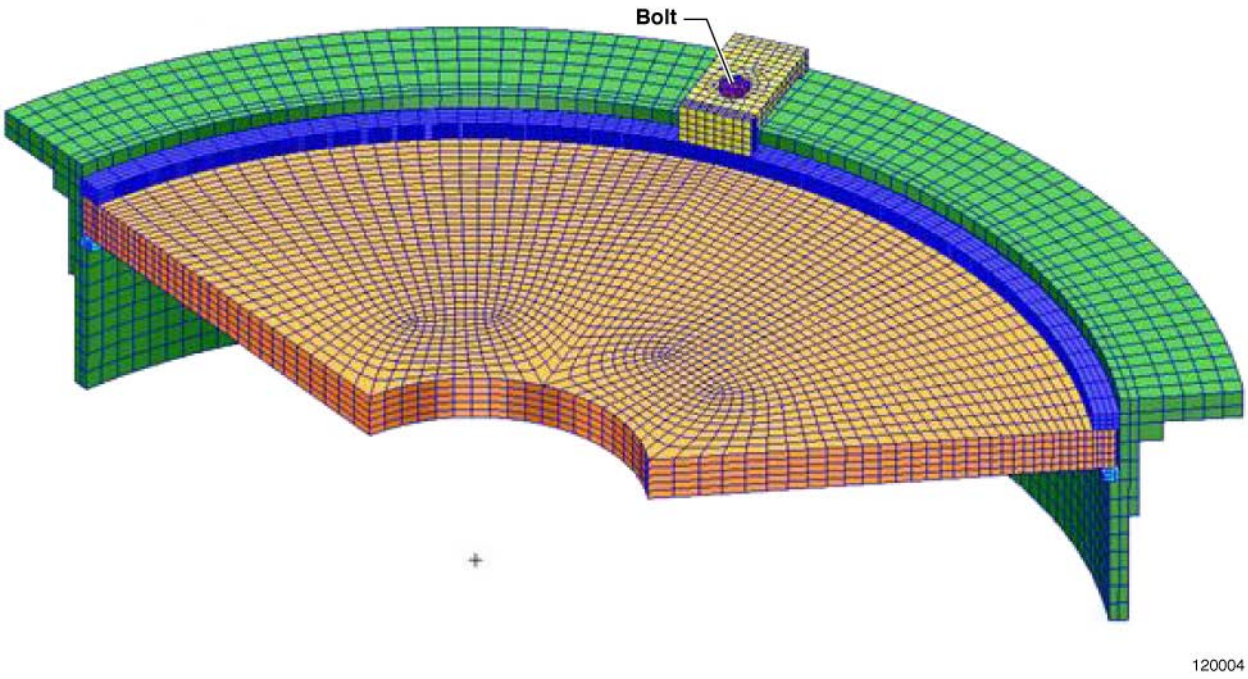

Figure 4(a). Contact body definition: clamp (yellow); spider mount (green); pressure ring (dark blue); Schmidt Plate (orange); and Schmidt Plate alignment ring (light blue, under the Schmidt Plate).

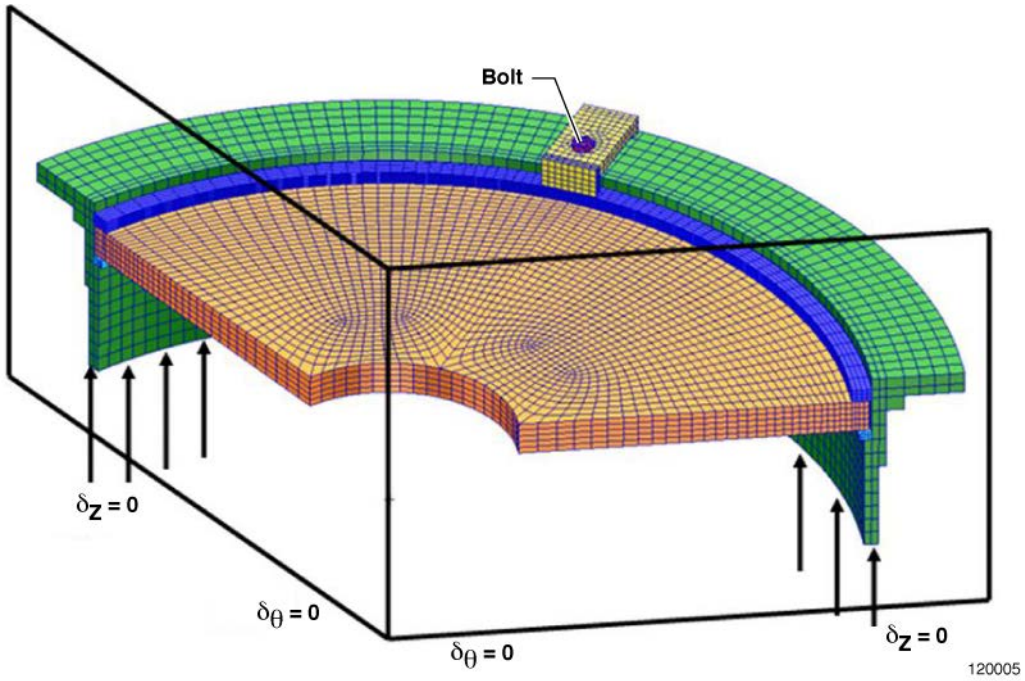

Figure 4(b). Mechanical constraints.

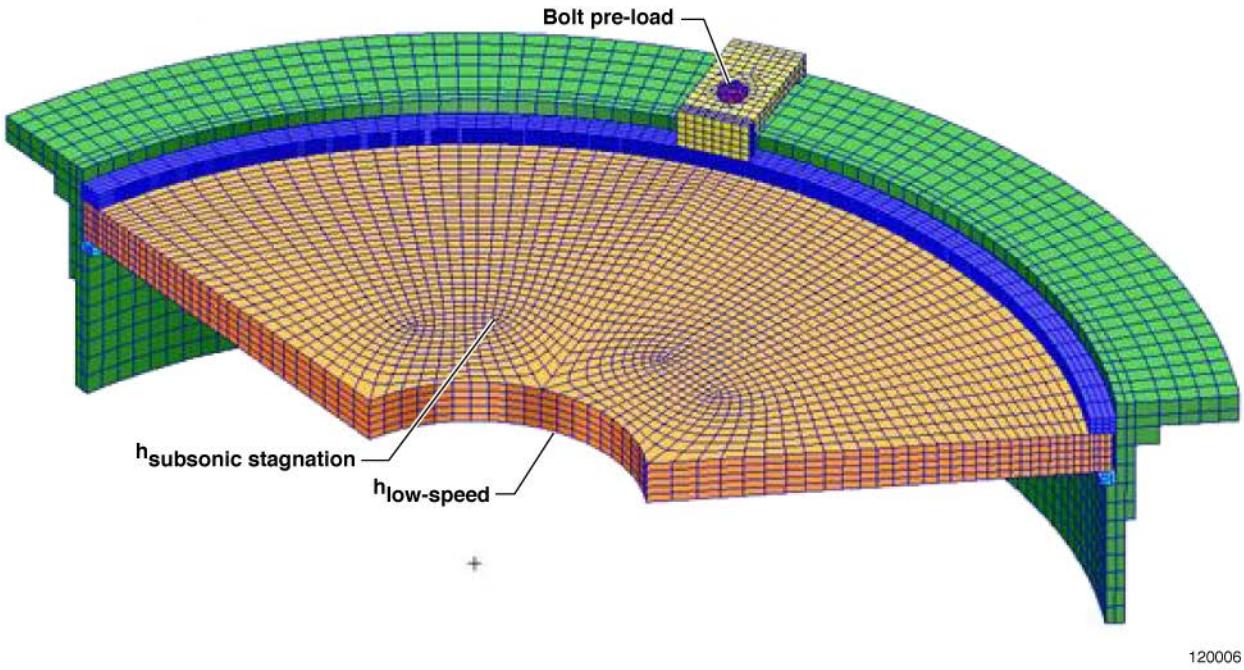

Figure 4(c). Thermal and mechanical loads.

Figure 4. The fine field imager front group 120-deg sector model mesh.

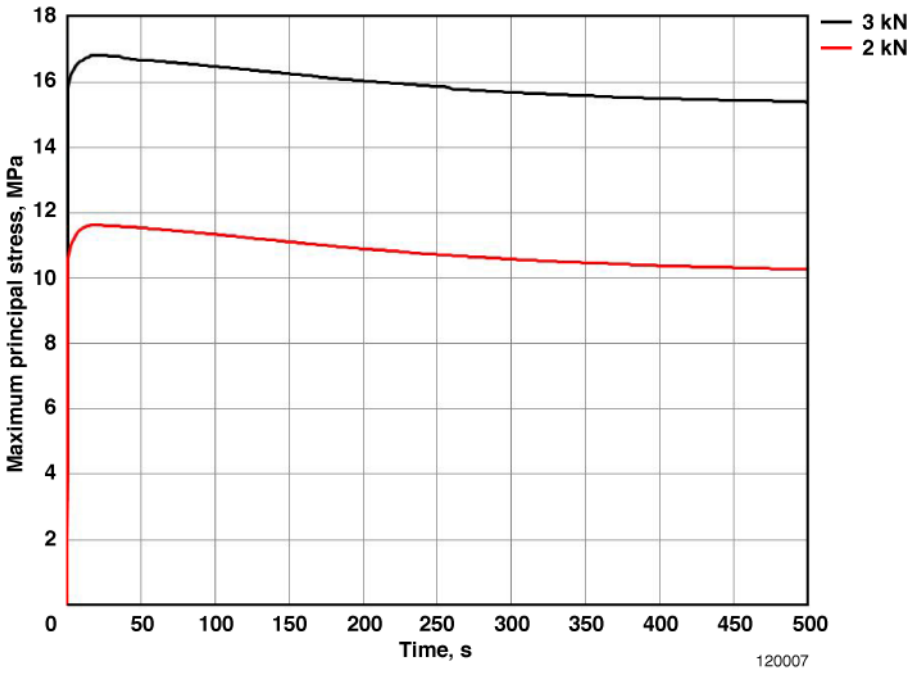

Figure 5. Maximum principal stress evolution sensitivity to variation in pre-load.

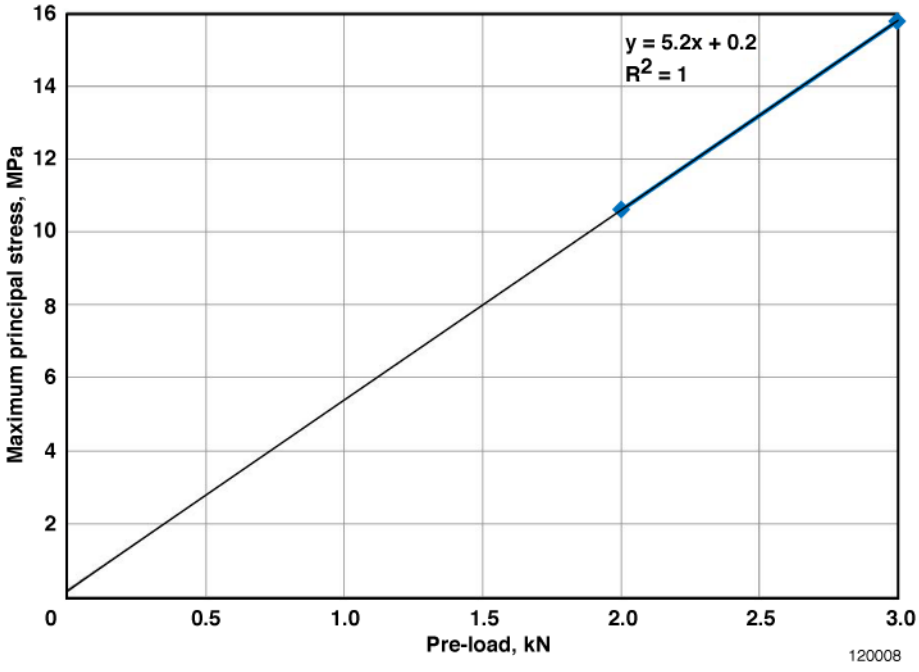

Figure 6. Comparison of maximum principal stress variation with pre-load.

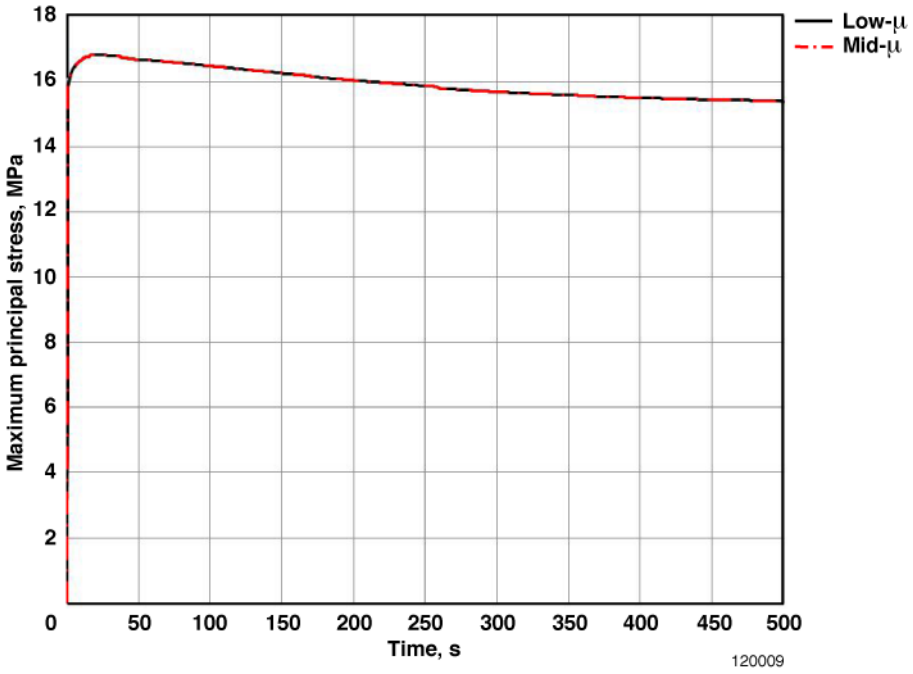

Figure 7. Maximum principal stress evolution sensitivity to variation in friction coefficients.

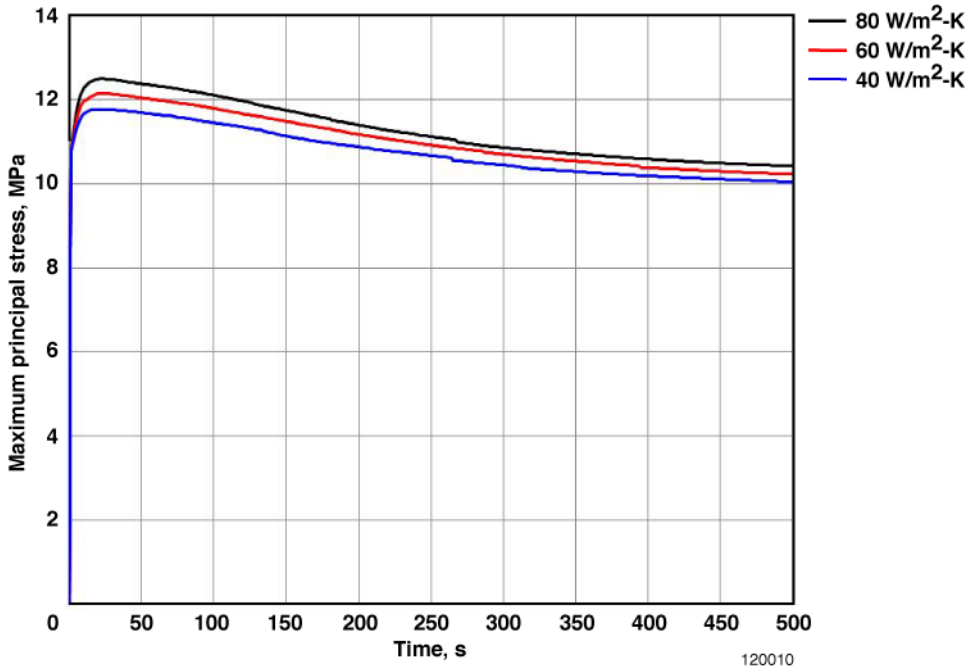

Figure 8. Maximum principal stress evolution sensitivity to variation in the convection coefficient.

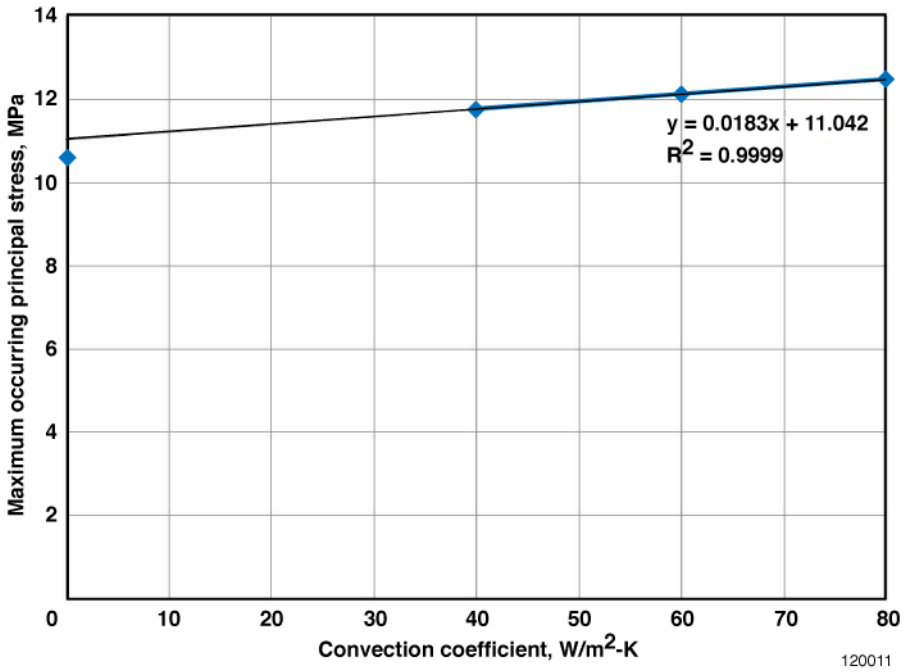

Figure 9. Evaluation of variation in convection coefficient and its effect on maximum principal stress at any time.

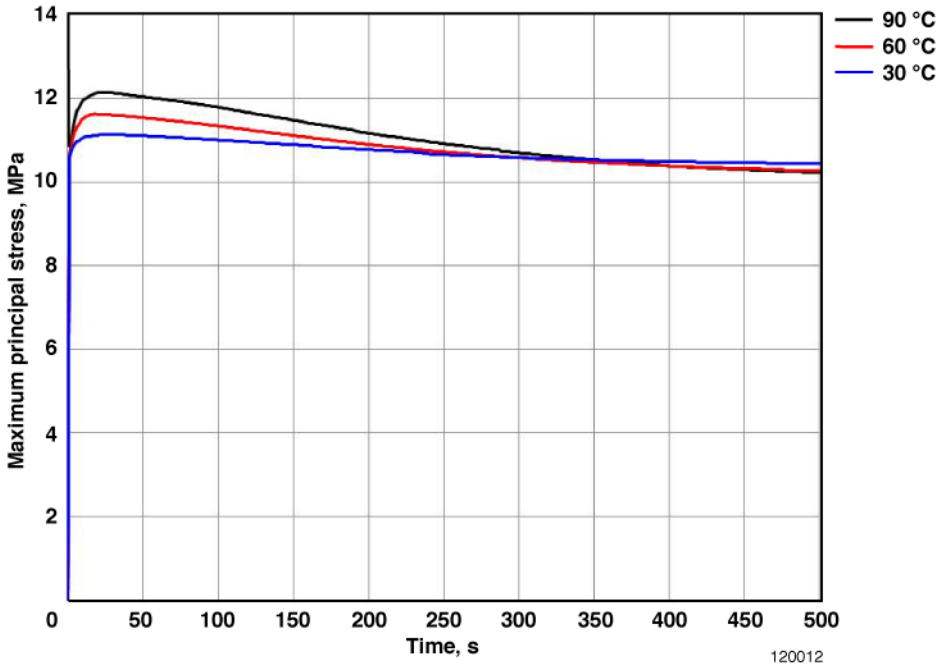

Figure 10. Maximum principal stress evolution sensitivity to variation in convective thermal shock strength (T_s - T_f).

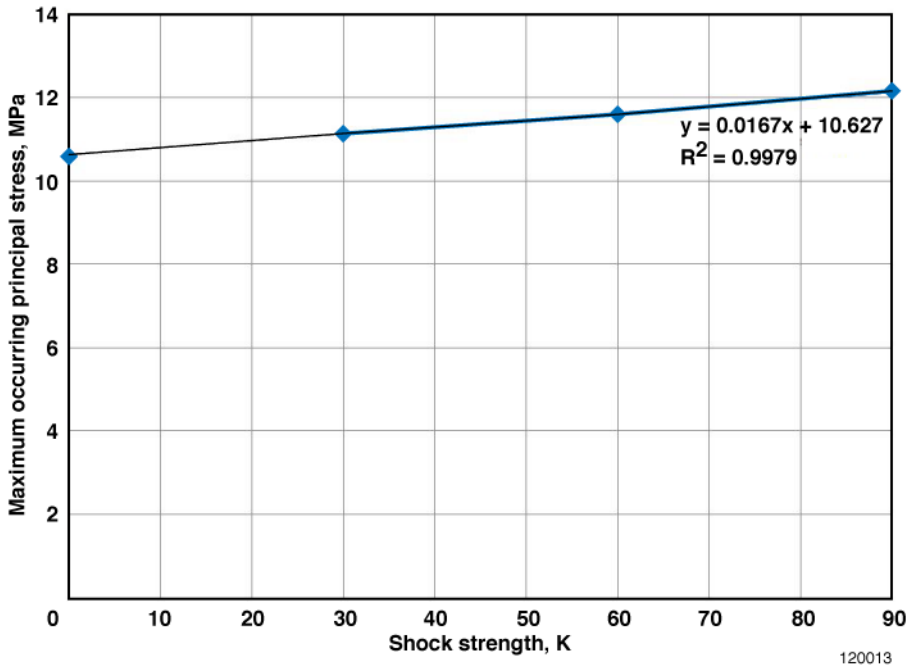

Figure 11. Evaluation of thermal shock strength effects on maximum principal stress at any time.

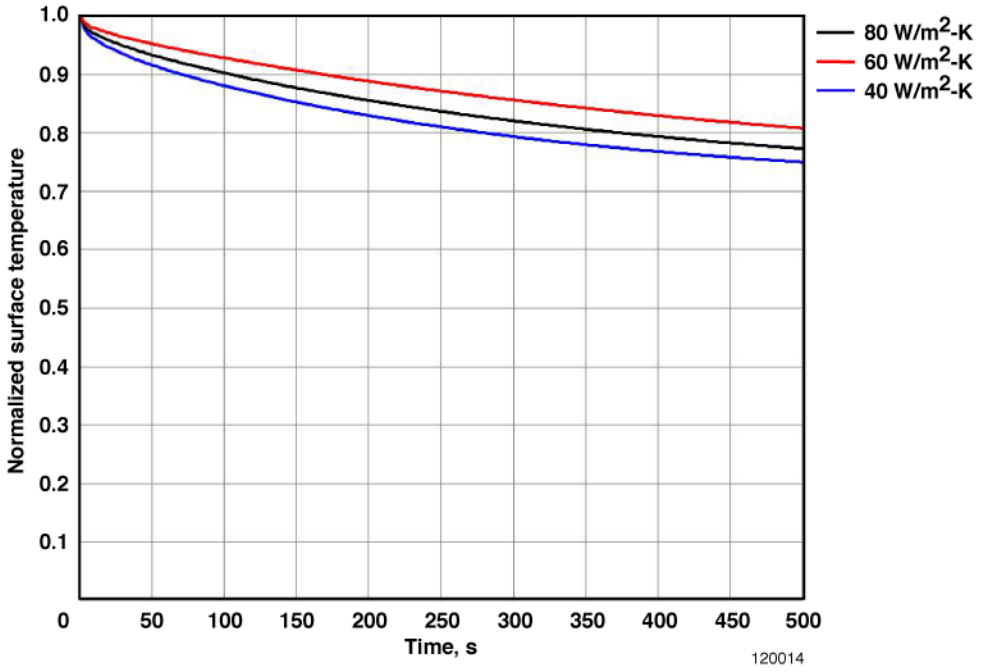

Figure 12. Variation in normalized surface temperature time history with convection coefficient.

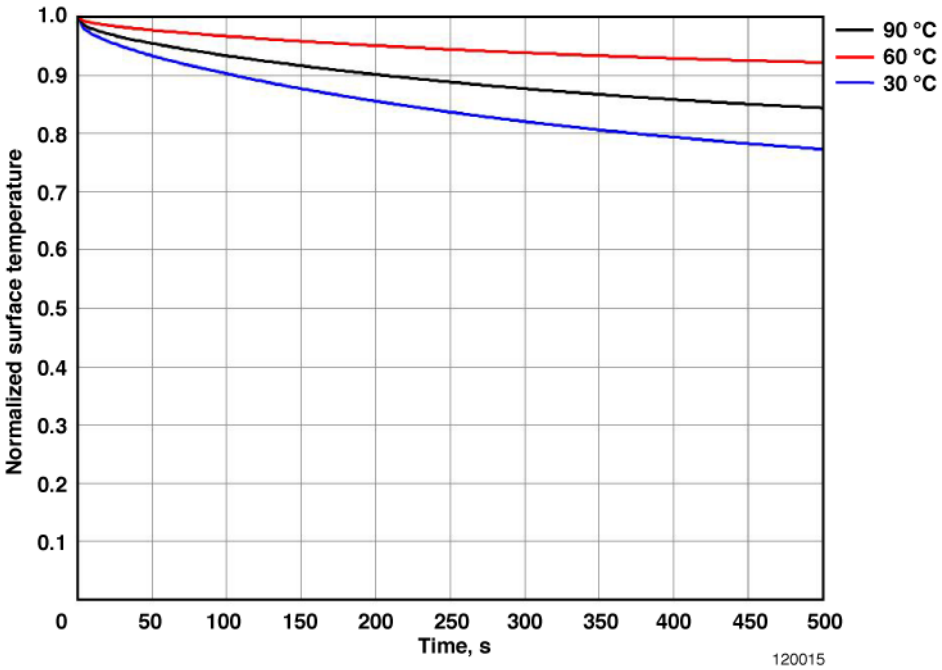

Figure 13. Variation in normalized surface temperature time history with thermal shock strength.

References

1. SCHOTT, "TIE-33: Design strength of optical glass and ZERODUR®," January 2009, http://www.us.schott.com/advanced_optics/english/download/tie-33_design_strength_of_optical_glass_and_zerodur_revb_us.pdf, accessed 1/27/2012.

2. Truitt, Robert Wesley, *Fundamentals of Aerodynamic Heating*, The Ronald Press Company, New York, 1960.

3. Incropera, Frank P., and David P. Dewitt, *Fundamentals of Heat and Mass Transfer*, 5th Edition, John Wiley & Sons, New York, 2002.